

Journal of Astronomical Telescopes, Instruments, and Systems

AstronomicalTelescopes.SPIEDigitalLibrary.org

Design and development of an adaptive optics system in visible and near-infrared for Inter-University Centre for Astronomy and Astrophysics 2-meter telescope

Jyotirmay Paul
Hillol K. Das
A. N. Ramaprakash
Mahesh Burse
Pravin Chordia
Kalpesh Chillal
Gaurav Datir
Bhushan Joshi
Pravin Khodade
Abhay Kohok
Vilas Mestry
Sujit Punnadi
Chaitanya Rajarshi
Chikku Shekhar

Jyotirmay Paul, Hillol K. Das, A. N. Ramaprakash, Mahesh Burse, Pravin Chordia, Kalpesh Chillal, Gaurav Datir, Bhushan Joshi, Pravin Khodade, Abhay Kohok, Vilas Mestry, Sujit Punnadi, Chaitanya Rajarshi, Chikku Shekhar, "Design and development of an adaptive optics system in visible and near-infrared for Inter-University Centre for Astronomy and Astrophysics 2-meter telescope," *J. Astron. Telesc. Instrum. Syst.* 5(3), 039002 (2019), doi: 10.1117/1.JATIS.5.3.039002.

SPIE.

Design and development of an adaptive optics system in visible and near-infrared for Inter-University Centre for Astronomy and Astrophysics 2-meter telescope

Jyotirmay Paul,^{a,b,*} Hillol K. Das,^b A. N. Ramaprakash,^b Mahesh Burse,^b Pravin Chordia,^b Kalpesh Chillal,^b Gaurav Datir,^b Bhushan Joshi,^b Pravin Khodade,^b Abhay Kohok,^b Vilas Mestry,^b Sujit Punnaadi,^b Chaitanya Rajarshi,^b and Chikku Shekhar^b

^aUniversity of North Bengal, High Energy and Cosmic Ray Research Centre, Siliguri, India

^bInter-University Centre for Astronomy and Astrophysics, Savitribai Phule Pune University, Pune, India

Abstract. Robo-AO is the first robotic autonomous laser-guided adaptive optics (AO) system operating in the sky. It is a very economical AO system especially suitable for observations with 1- to 3-m class telescopes. A second Robo-AO system, which works both in the visible and near-infrared wavelengths, has been developed to improve the image quality of the 2-m diameter telescope at Inter-university Centre for Astronomy and Astrophysics Girawali Observatory in India. We present the optomechanical design and development of the Laser Guide Star Facility (LGSF) and the Cassegrain AO facility with various test results. Effects of different projection geometries of the LGSF have been discussed with modeling results. Comprehensive study of an atmospheric dispersion corrector with dispersion model and development of a generic software are elaborated with experimental results. Toward the end, AO loop test results in the presence of artificial turbulence generated in the laboratory are presented. © The Authors. Published by SPIE under a Creative Commons Attribution 4.0 Unported License. Distribution or reproduction of this work in whole or in part requires full attribution of the original publication, including its DOI. [DOI: [10.1117/1.JATIS.5.3.039002](https://doi.org/10.1117/1.JATIS.5.3.039002)]

Keywords: atmospheric effects; adaptive optics; polarization; high angular resolution; imaging techniques; laser guide star; atmospheric dispersion corrector; miscellaneous.

Paper 18108 received Nov. 6, 2018; accepted for publication Jun. 24, 2019; published online Jul. 25, 2019.

1 Introduction

The technique of adaptive optics (AO) is used in astronomy to improve the performance of optical/near-infrared (NIR) telescopes by compensating for the effects of wavefront distortions, which are introduced when light from a distant astronomical source passes through the turbulent atmosphere of Earth.

As per record, it was Babcock who first proposed the concept of AO in the year 1953,¹ and about two decades later, with the advent of computers, the first “real-time wavefront correction system” was proposed.^{2,3}

The past few decades have witnessed the commissioning of several large telescopes, and we are now talking of extremely large telescopes, e.g., the Thirty Meter Telescope, the Giant Magellan Telescope, and the Extremely Large Telescope. The atmospheric turbulence seriously limits their performance, limiting their angular resolution to $\approx \lambda/r_0$, where r_0 is the Fried parameter, e.g.,⁴ which quantifies the coherence length scale of the atmosphere. The sensitivity of the telescope for point sources fainter than the sky background also grows only as the square of the telescope diameter⁵ unlike as the fourth power of the diameter as in a turbulence-free/compensated environment.

AO has great potential in upgrading the performance of moderate-sized telescopes. Several moderate-sized telescopes in the range 1- to 3-m diameter apertures have been upgraded with AO facilities, e.g., at Mount Wilson, Lick Observatory, and very recently with the Robo-AO on P60 telescope at Palomar Observatory and the 2-m telescope at Kitt Peak National Observatory.

Robo-AO^{6–10} was a joint collaborative venture between the California Institute of Technology and the Inter-university Centre for Astronomy and Astrophysics (IUCAA), India. After successful performance of Robo-AO at the two observatories,^{11,12} it was decided to make a similar AO system for the IUCAA 2-m telescope keeping the core characteristics of the system as it is while introducing some improvements. The AO system was christened iRobo-AO in keeping with its predecessor’s name.

Section 2 of the paper is dedicated to the complete system description, which is further subdivided into different subsections. While, in Sec. 2.1, we discuss the Laser Guide Star Facility (LGSF) at length, Sec. 2.2 discusses the different projection geometry of the LGSF and their effects and Sec. 2.3 explains the main Cassegrain AO facility and its various components. Finally in Sec. 3, we discuss the wavefront reconstruction structure of iRobo-AO followed by a laboratory demonstration of the AO loop test.

2 System Description

The iRobo-AO comprises two main subsystems: (a) the LGSF mounted at the side of the telescope and (b) the Cassegrain AO facility mounted at the Cassegrain focus of the telescope.

2.1 Laser Guide Star Facility

Fine sampling of the wavefront by the wavefront sensor (WFS) is required for optimal correction by the AO system, and this requires a good amount of photons to be incident across its working aperture. The need for a bright guide star close to the target star is therefore imperative.⁴

Owing to the lack of sufficiently bright natural guide stars (NGSs) close enough to every target in the sky, AO systems

*Address all correspondence to Jyotirmay Paul, E-mail: jpaul@iucaa.in

cannot function in all directions of the sky. This poses a serious limitation to AO corrections. To overcome this limitation Foy and Labeyrie¹³ suggested an alternative technique, the creation of an artificial guide star in the sky using a laser; the LGS remains within the isoplanatic angle and in spite of some cone effect limitations it increases the sky coverage, thereby overcoming the limitation set by the unavailability of bright NGS.

iRobo-AO uses the Rayleigh backscattered light from an ultraviolet (UV) LGS for wavefront correction. The brightness of the Rayleigh scattered guide stars depends on the density of the air molecules present at a given altitude and it falls exponentially with altitude. iRobo-AO LGSF is optimized for a moderate height of 10 km.

The laser projector is made of a UV laser, an external shutter, one fast steering mirror (FSM), a fold mirror (FM), one convex lens, and planoconvex projector lens. Each component of the laser projector system (Fig. 1) is briefly explained below. The specification of all the optics is given in Table 1.

The core of the laser projector system is a Q-switched UV laser (10 W at 355 nm, with a pulse width of 33 ns and 10-kHz repetition rate) mounted in an enclosed projector assembly. A separate chiller is used to circulate cold water through the laser so that the laser diode temperature is maintained at an optimum level.

As the laser is of type class IV, an additional external dielectric laser shutter is used to facilitate emergency shutdown irrespective of the internal laser shutter.

Flexures and alignment errors of the LGSF could lead to an error in pointing of the LGS in the sky. The FSM is used to compensate for any mechanical pointing error so that all the subapertures on the primary mirror are adequately illuminated. The FSM has a laser line UV-coated mirror at 355 nm mounted on it with a maximum mechanical stroke of ± 26 mrad, which corresponds to $\pm 1.89'$ in the sky.

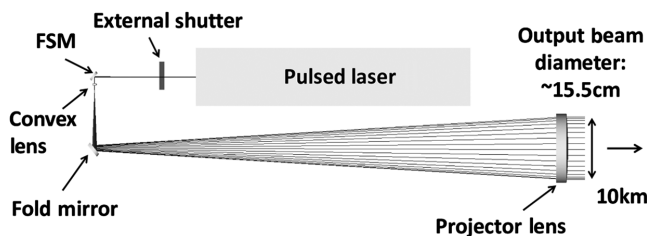


Fig. 1 Optical layout of the laser projector.

Table 1 Specification of laser projector optics.

Name of optics	Specification
FSM, FM	Diameter: 25 mm, material: fused silica
Convex lens (off the shelf)	ROC ^a : ± 14.4 mm, center thickness: 5.9 mm; material: fused silica; diameter: 12.7 mm; focal length: 15 mm
Projector lens (custom-made)	Planoconvex ROC: 727.39 mm, center thickness: 35 mm material: corning HPFS grade 1A (C79-80), diameter: 165 mm, conic constant: -0.58759 , focal length: 1.527 m

^aROC: Radius of curvature.

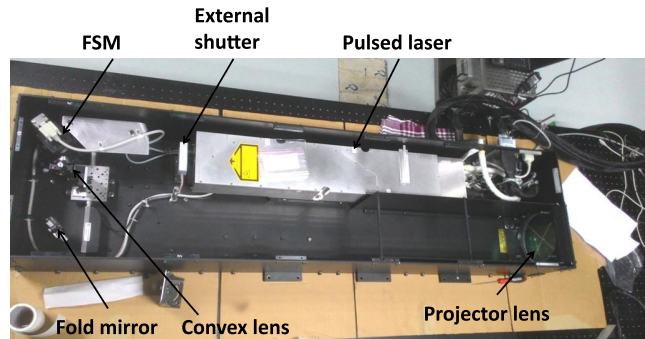


Fig. 2 Laser projector assembly (length: 1.5 m, width: 0.37 m, height: 0.2 m, and weight: 65 kg).

A UV-coated convex lens mounted on a linear actuator expands the laser beam to fill the entire projector lens. The stage is computer-controlled and can be used to focus the LGS.

A laser line mirror coated at 350 nm is then used to fold the beam toward the projector lens. The folded geometry using the FSM and the FM makes the laser projector very compact.

The main projector lens is a planoconvex lens of diameter 165 mm and is custom-made from UV-grade fused silica; this lens is slightly aspheric and it focuses the output laser beam at a suitable height of about 10 to 12 km.

The complete assembly of the laser projector is shown in Fig. 2.

2.1.1 Periscope

The laser projector is mounted on the side of the telescope, as shown in Fig. 3. The emanating beam bends twice near the top of the telescope so that the beam is launched into the sky from the back of the secondary mirror. The periscope system consists of two custom-made 250-mm diameter laser line-coated mirrors. One of the mirrors is mounted on the upper rim of the telescope just above the laser projector, which reflects the laser light from the projector toward the second mirror mounted behind the cover at the back of the secondary mirror. With the help of the periscope the laser beam can be fired axially with respect to the telescope. This is advantageous as explained in the next section. Figure 4 shows the laser beam being test-fired from IUCAA Girawali Observatory (IGO)—the photograph was taken with a U-filter mounted in front of a modified digital single-lens reflex camera.

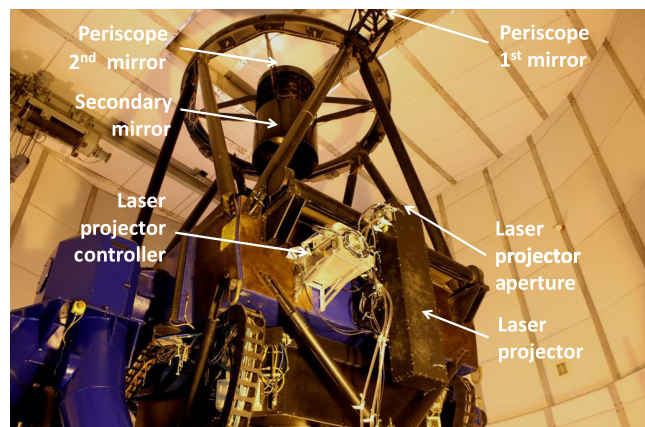


Fig. 3 Laser projector mounted on telescope.



Fig. 4 LGSF test-fired from IGO.

2.2 Viewing Geometry Dependence of Laser Beacons

The shape of the laser spot will not be identical in all the subapertures for large telescopes because of the viewing geometry. As the subapertures move away from the projection axis, the spots appear more elongated. This situation has been discussed at length by several authors, e.g., Refs. 4, and 14–16.

Here, we compare the two possibilities of laser projection geometries—projected from behind the secondary and from the side of the telescope; irrespective of the projection geometry, some of the spots will appear elongated. A simulation was done to determine the radial elongation of the laser spots across various subapertures because of the viewing geometry, under the two cases.

2.2.1 Simulation

The first requirement in doing so is to estimate the approximate number of backscattered photons from the LGS per subaperture (n_p) reaching the WFS. This was estimated following Hardy⁴ and using the Lidar relation as in Eq. (1), which was originally given by Gardner et al.¹⁷ All the parameters used are given in Table 2 with their values and units. Here, $\sigma_B N(z)$ (m^2) is the effective backscatter cross section and $N(z)$ (m^{-3}) is the number density of scatterers at range z . Note that, $\sigma_B N(z)$ for various z and wavelengths are presented in a tabular format in Hardy⁴ and Δz typically varies from 100 to 400 m.^{18–21}

$$n_p = \left(\frac{\lambda_B}{hc} \right) T_A^2 \frac{\sigma_B N(z)}{4\pi} \left(\frac{\Delta z}{z^2} \right) (ET_L d^2 T_0). \quad (1)$$

Using Eq. (1) and Table 2 we get 34.639 photons/pulse/subaperture, and considering 1 ms exposure we get about ≈ 346 photons per subaperture.

Figure 5 shows the viewing geometry of the laser beacon. It can be seen that the elongation will progress in a radial direction from the projection axis. Considering an ideal situation where there is no elongation, we find from Zemax Optical Design Software that the spot size diameter of a single lenslet of the lenslet array-Shack–Hartmann wavefront sensor (SHWFS) (refer WFS in Sec. 2.3) image on the WFS camera to be $36 \mu\text{m}$ using Zemax FFT PSF cross-section subroutine. Assuming the spot to be symmetric and Gaussian in nature, we equate this to $6\sigma_{\text{org}}$ (i.e., $\pm 3\sigma_{\text{org}}$ range) cutoff, where σ_{org} is the standard deviation of

Table 2 Parameter and their values for estimating n_p .

Parameter	Value
Laser beacon wavelength, λ_B	0.355 μm
One-way transmission of atmosphere between telescope and beacon (at 10 km and 45 deg), T_A	0.36
Rayleigh backscatter parameter, $\sigma_B N(z)^a$	27.2 photons per million meters
Received range gate length, Δz	400 m
Range to the center of the range gate, z	10 km
Laser power	10 W
Pulse repetition rate	10^4 Hz
Pulse energy, E	10^{-3} J
Transmission of laser path to projection aperture, T_L	0.8855
Subaperture size at telescope entrance pupil, d	0.181 m
Transmission of laser path from primary mirror to WFS, T_0	0.6025

^aThe product of the two parameters $\sigma_B N(z)$ was obtained from Hardy.⁴

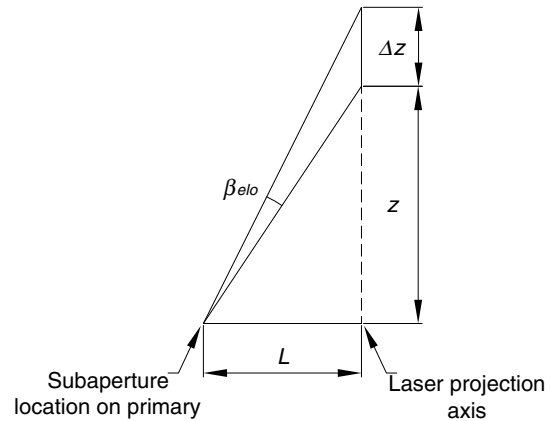


Fig. 5 LGS elongation at a distance L from the laser projection axis.

the spot size without any elongation. For a $24\text{-}\mu\text{m}$ pixel size of the camera, we obtain

$$\sigma_{\text{org}} = 0.25 \text{ pixel}. \quad (2)$$

The angular size of the elongation (Fig. 5), β_{elo} , was estimated by Ref. 22 to be

$$\beta_{\text{elo}} \approx \left(\frac{\Delta z \times L}{z^2} \right) \left(\frac{206265 \times P_s}{24} \right) \text{ pixel}, \quad (3)$$

where P_s , the plate scale on the WFS camera, is $32.4 \mu\text{m}/''$ and L is the distance of the subapertures (on the primary) from

the laser launch point; the maximum value of L for off-axis and on axis projections are 2 and 1 m, respectively, in our case.

The standard deviation of this elongated spot, σ^* , again considering a Gaussian distribution [6 STD (i.e., ± 3 STD) range] can be approximated to one-sixth of β_{elo} and the effective standard deviation of the elongated laser spot along the direction of elongation is given as

$$\sigma_{\text{elo}} = \sqrt{\sigma^{*2} + \sigma_{\text{org}}^2} \text{ pixel.} \quad (4)$$

The angular variation of the elongated spot at various subapertures can be estimated as follows. We define the laser projection coordinate as $(x_{\text{center}}, y_{\text{center}})$ with respect to the subaperture coordinate (x, y) . The rotation angle of the spot is defined as

$$\gamma = \tan^{-1} \left(\frac{y - y_{\text{center}}}{x - x_{\text{center}}} \right). \quad (5)$$

The covariance matrix for a two-dimensional Gaussian distribution, whose major and minor axes are axially aligned to the frame of reference, can be written as

$$\text{COV}_{\text{matrix}} = \begin{bmatrix} \sigma_{\text{elo}}^2 & 0 \\ 0 & \sigma_{\text{org}}^2 \end{bmatrix}.$$

When the spot is rotated by γ , the general covariance matrix can be rewritten as

$$\text{COV}_{\text{gen}} = R(\gamma) \text{COV}_{\text{matrix}} R(\gamma)^T, \quad (6)$$

$$\text{COV}_{\text{gen}} = \begin{bmatrix} a & b \\ c & d \end{bmatrix}, \quad (7)$$

where $R(\gamma)$ is the rotator matrix

$$R(\gamma) = \begin{bmatrix} \cos(\gamma) & -\sin(\gamma) \\ \sin(\gamma) & \cos(\gamma) \end{bmatrix}, \quad (8)$$

and the covariance matrix elements are

$$\begin{aligned} a &= \sigma_{\text{elo}}^2 \cos^2 \gamma + \sigma_{\text{org}}^2 \sin^2 \gamma \\ b &= (\sigma_{\text{elo}}^2 - \sigma_{\text{org}}^2) \sin \gamma \cos \gamma \\ c &= b \\ d &= \sigma_{\text{elo}}^2 \sin^2 \gamma + \sigma_{\text{org}}^2 \cos^2 \gamma. \end{aligned}$$

Using the Python random number generator routine “`numpy.random.multivariate_normal(mean, COVgen, np)`” [this Python routine draws n_p number of random samples from a multivariate normal distribution centered at “mean” and having generalized variance (“COV_{gen}”) with respect to an arbitrary axis] and Eq. (7), n_p photons are randomly distributed within each subaperture where the mean position of the distribution is the subaperture center. This was done for both the coaxial ($0 \leq L \leq 1$, $0 \leq \gamma \leq 2\pi$) and the side ($0 \leq L \leq 2$, $0 \leq \gamma \leq \pi$) projection geometries.

The simulated results are presented in Figs. 6 and 7 where the red spot represents the laser projection axis and the square array represents a total of 11×11 subapertures. It can be seen that as we move outward from the point of projection the spots elongate

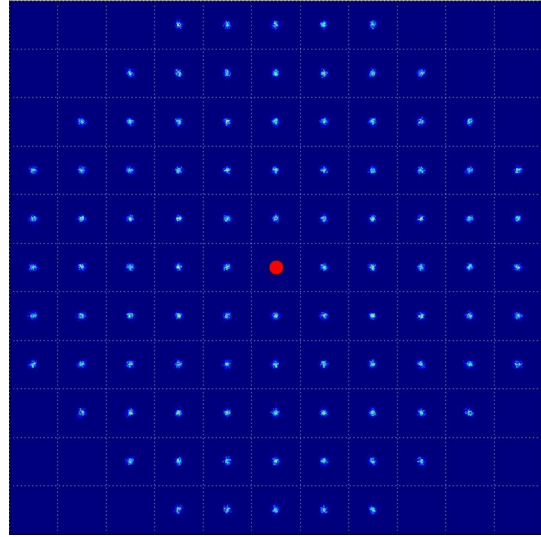


Fig. 6 Array of LGS spots on each subaperture for coaxial laser projection (red spot is the projection axis).

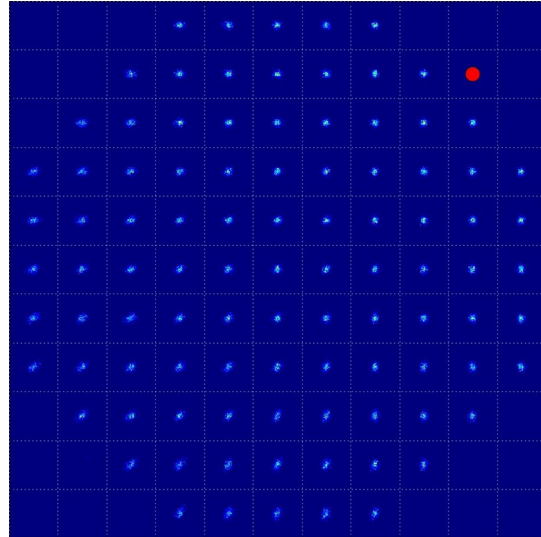


Fig. 7 Array of LGS spots on each subaperture for laser projection from telescope side (red spot is the projection axis).

radially and more so for the side projection geometry; the maximum elongation for coaxial and side projections was estimated to be $\sim 1.2''$ and $\sim 2''$ for our case. As discussed by Hardy (1998),⁴ elongation of laser spots is a significant contributor to WFS measurement errors and also errors due to angular isoplanatism. In the iRobo-AO system, these errors for a side projection geometry will be ≈ 1.67 times more than that for on-axis projection. Hence we have opted for on-axis laser projection.

2.2.2 Focusing mechanism

It is extremely important for the LGS to be well focused in the sky. To achieve this, the biconvex lens mounted on a high-precision linear actuator in the laser projector is moved along the laser projector optical axis. Figure 8 shows the difference of the beam diameter across 22-m separation between the projector

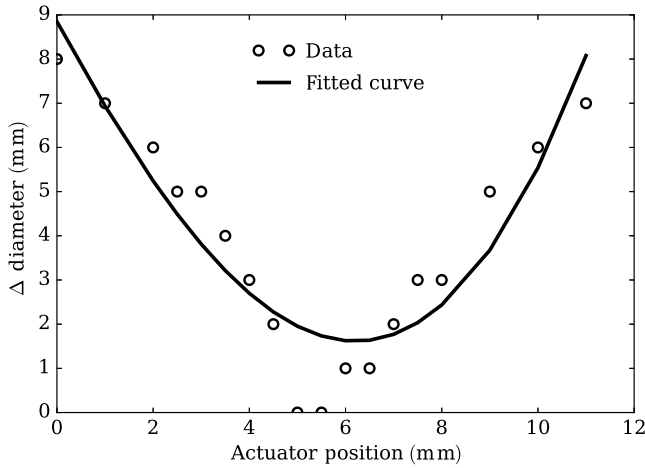


Fig. 8 Beam diameter change across 22 m for various actuator positions.

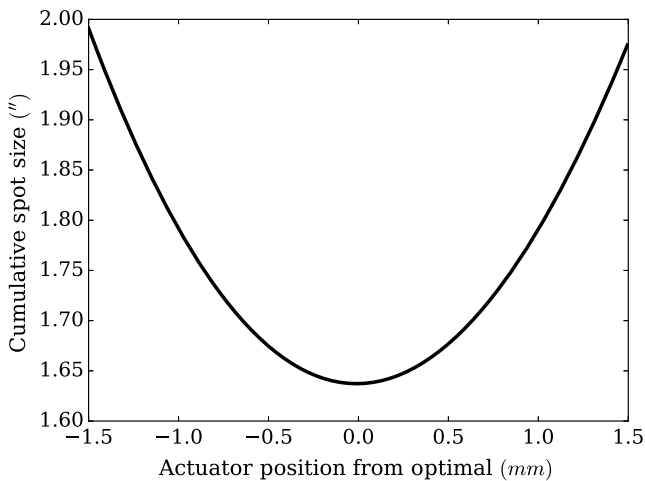


Fig. 9 Cumulative effect on the LGS blurring considering both seeing and effects of various actuator positions as per Zemax.

lens and the screen for various actuator positions; the difference is minimum for an actuator position of ~ 6 mm.

The seeing limited spot width of the LGS at 10 km will be around $1.629''$ at $0.355\text{-}\mu\text{m}$ wavelength. Cumulative effect in the spot size is generated by the quadrature addition of the pure blurring of the LGS due to the defocusing and the seeing limited spot. An LGS width of up to $\approx 2'$ (half of the subaperture at CCD39 WFS camera, Sec. 2.3—wavefront sensor) is within the acceptable range. The cumulative spot diameter of the LGS at 10 km due to the translation of the convex lens from the optimal position by the precession actuator is given in Fig. 9. The actuator has a stepping resolution of $0.10\ \mu\text{m}$, which is more than adequate to focus the LGS within the required spot size at 10 km.

2.3 Cassegrain AO Facility

The Cassegrain facility primarily consists of three arms: two science arms working in the visible and infrared (IR) and a wavefront sensing UV arm. The entire optical relay system is shown in Fig. 10. It mainly consists of five off-axis parabolic (OAP) mirrors, a deformable mirror (DM), a tip-tilt correcting mirror

(TTM), a pair of rotating prisms used as atmospheric dispersion corrector (ADC), and two dichroic filters to split up the light into various bands. Apart from these, it also has an electron multiplying charged-couple device (EMCCD) camera, a fast readout UV-sensitive wavefront sensing CCD39 camera and an infrared camera (IR cam), which is indigenously developed at IUCAA (details of the IR cam will be presented in our forthcoming paper). The dimension of the entire Cassegrain box is about $1\ \text{m} \times 0.8\ \text{m} \times 0.2\ \text{m}$.

A brief introduction of all the elements that are assembled in the Cassegrain facility are given here with specifications of the optics in Table 3.

Telescope simulator. An internal telescope optics simulator is also an integral part of iRobo-AO. The entire optical alignment of iRobo-AO has been done using the simulator. It has the capability of simulating two foci—one for a UV source at a finite height of say 10 km above the telescope and second for a source at infinity in the visible band. In both cases, the f /number is matched with that of the telescope beam. FM1 mounted on a linear stage is used to direct the light from the telescope into the main AO system. Figure 11 shows the optical layout of telescope simulator, it can be seen that the UV (LGS) focus and the visible (target) focus are separated by 40 mm with $f/10$ beam as in the case with telescope optics.

OAP mirrors. iRobo-AO uses five custom-made OAP mirrors to relay light from the telescope focus to the various components of the visible, IR, and UV arms. They also help in reimaging the telescope entrance pupil on the DM, the ADC, and the WFS.

Deformable mirror. The entrance pupil of the telescope is first reimaged on the DM surface across its clear working aperture of 4.4 mm. The atmospheric turbulence demands a stroke size of [Eq. (5)]²³

$$\delta = \frac{3\lambda}{2\pi} \sqrt{l} \left(\frac{D_{\text{pupil}}}{r_0} \right)^{5/6}, \quad (9)$$

where $l = 1.03$ if the DM compensates for the tip-tilt plus higher-order aberrations and is equal to 0.134, if tip-tilt is separately accounted for and removed, say using the TTM. Here, D_{pupil} is the telescope entrance pupil diameter. It can be seen from the equation that as r_0 varies as $\lambda^{6/5}$, the DM stroke is wavelength-independent.

At IGO for $r_0 \approx 7.6\ \text{cm}$ at $\lambda = 0.550\ \mu\text{m}$, the net stroke required for the complete aberration correction is $\approx 4\ \mu\text{m}$ and $\approx 1.5\ \mu\text{m}$ with separate tip-tilt correction. The Boston Micromachines' MEMS-based DM with a maximum stroke size of $3.5\ \mu\text{m}$, clear aperture of 4.4 mm, and a total of 140 working actuators was selected for iRobo-AO to handle the higher-order corrections only.

Dichroic filters. A set of two dichroic filters are used to split the input beam into the UV, visible, and IR arms (more details are given in Sec. 2.3.1).

Filters. Two motorized filter wheels each with six slots are mounted in front of the EMCCD science camera. A set of Bessell U, B, V, R, and I filters are mounted in the slots. The rest of the slots will be populated as per future requirements.

Atmospheric dispersion corrector. The atmospheric dispersion also imparts serious effects, especially when observing objects at large zenith angles. In such cases, the images of the objects generally tend to elongate due to dispersion. The ADC performance is discussed at length in Sec. 2.3.2.

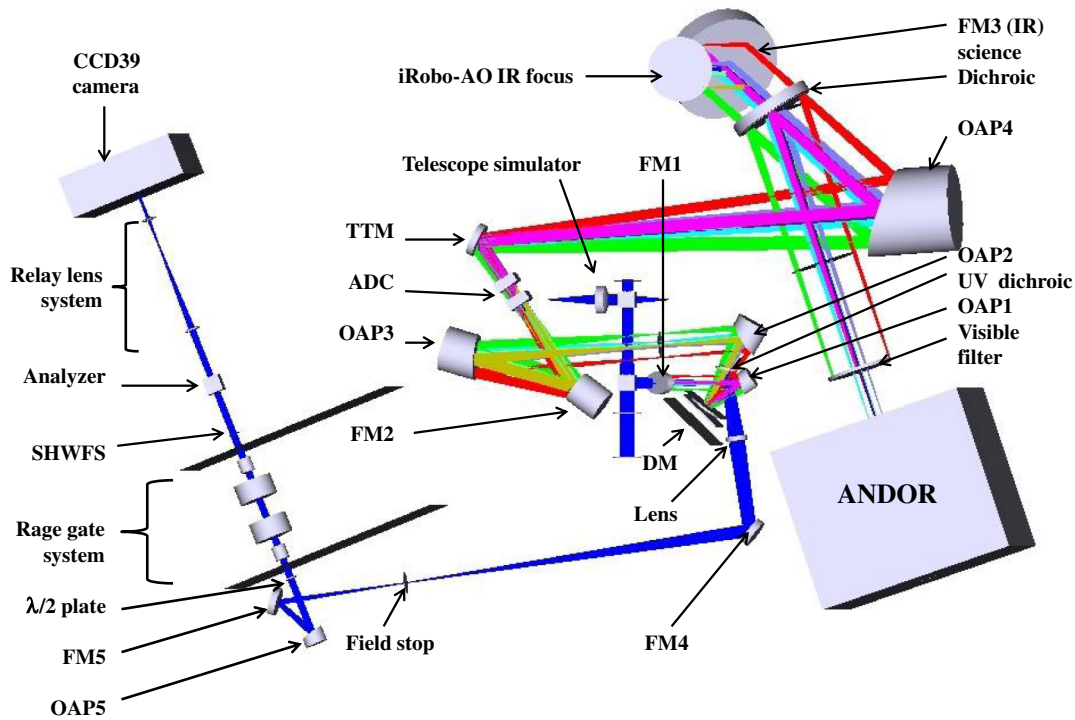


Fig. 10 iRobo-AO optical layout.

Table 3 Specification of iRobo-AO Cassegrain optics.

Name of optics	Specification
FM1 (elliptical)	Major and minor diameters: 35.3 and 20 mm Thickness: 2 mm, material: fused silica (UV grade)
OAP1 ^a	OAD ^b : 23.556 mm, Parent ROC ^c : 78.056 mm, material: Zerodur
DM (MEMS-based)	Aperture: 4.4 × 4.4 mm ² , continuous surface Stroke: 3.5 μm, Actuators: 140
UV arm optics	
Laser dichroic	Diameter: 22 mm, thickness: 2 mm, reflects 355 nm, and transmits 390 to 2500 nm
Lens	Surface1, ROC: 141.669 mm (convex) Surface2, ROC: 80.1968 mm (convex) Center thickness: 5 mm, diameter: 19 mm Material: fused silica (UV grade)
FM4,5	Diameter: 25.4 mm, material: fused silica (UV grade)
OAP5	OAD: 68.812 mm, parent ROC: 303.086 mm, material: Zerodur
Retarder	Retardation: λ/2 at 355 nm, Size: 10 × 10 × 1.6 mm ³ Material: quartz

Table 3 (Continued).

Name of optics	Specification
Pockels cell	BBO Pockel cell at 355 nm, aperture: 6 mm
SHWFS	Planoconvex, focal length: 76.6 mm @ 633 nm Lenses array: 11 × 11, each lenslet size: 0.5 × 0.5 × 1 mm ³
Analyzer	Polarizing cube beam splitter, 15 × 15 × 15 mm ³ Material: fused silica (UV grade)
Relay lens1	Surface1, plane, surface2, ROC: 38.6 mm (convex) Center thickness: 2 mm, diameter: 15 mm Material: fused silica (UV grade)
Relay lens2	Surface1,2 ROC: ±21.5 mm (convex), center thickness: 3.1 mm Material: fused silica (UV grade), diameter: 15 mm
Visible and IR arms optics	
OAP2	OAD: 62.648 mm, parent ROC: 118.919 mm, material: Zerodur
OAP3	OAD: 57.595 mm, parent ROC: 326.64 mm, material: Zerodur
OAP4	OAD: 304.468 mm, parent ROC: 730.583 mm, material: Zerodur

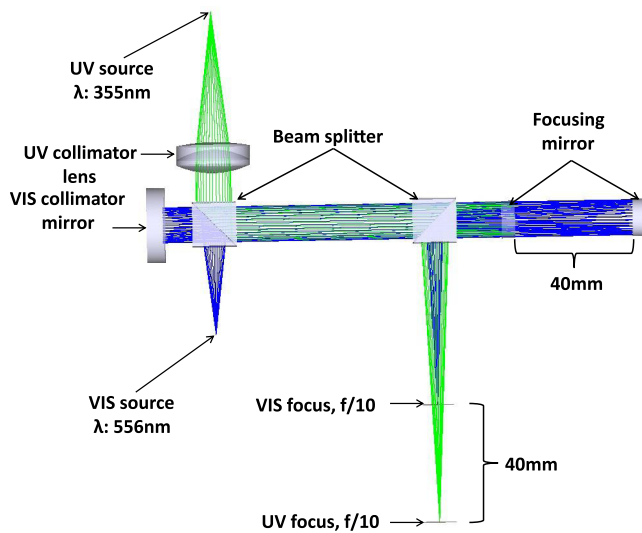
Table 3 (Continued).

Name of optics	Specification
FM2,TTM	Diameter: 30 mm, material: Zerodur
ADC	IGO specific design (Fig. 15)
Science dichroic	Diameter: 76 mm, thickness: 10 mm Reflects visible (390 to 900 nm) and Transmits NIR spectrum (900 to 2500 nm)
FM3	Diameter: 101.6 mm, thickness: 19.1 mm, material: fused silica Coating: protected gold (700 to 10,000 nm)
Visible filters	Bessell U, B, V, R, and I, diameter: 25 mm, thickness: 5 mm

^aOAP: Off-axis parabolic mirror.

^bOAD: Off-axis distance.

^cROC: Radius of curvature.

**Fig. 11** Optical layout of telescope simulator.

Tip-tilt mirror. Tip-tilt correction is the lowest-order AO correction, only when $r_0 \approx D_{\text{pupil}}$; for $D_{\text{pupil}} > r_0$, there is lesser power in the tip-tilt.^{24,25} The presence of a NGS (can be fainter than the LGS), however, is a must for tip-tilt correction. LGSs cannot be used for this purpose because, after the two-way travel of laser lights through the atmosphere, the tip-tilt information is lost. The overall one-axis tilt variance is given as⁴

$$\alpha_{\text{tilt}}^2 = 0.184 \left(\frac{\lambda}{D_{\text{pupil}}} \right)^2 \left(\frac{D_{\text{pupil}}}{r_0} \right)^{\frac{5}{3}} \text{rad}^2. \quad (10)$$

The net angular tilt considering ± 3 sigma variation will be $\approx 11 \mu\text{rad}$ for IGO parameters; this is the overall tilt of the wavefront in one axis at the primary mirror. With an angular magnification of the beam at the TTM of ≈ 95 , the overall atmospheric tilt after magnification at TTM will be $\approx 1 \text{ mrad}$. Hence the

chosen piezo tip-tilt platform with a maximum stroke of 2 mrad is sufficient for our purpose.

Both the ADC and TTM are common to the visible and IR arms. It needs to be mentioned here that although a TTM is an integral part of iRobo-AO, it can be used to its full capacity only after the IR camera is commissioned. Either the EMCCD visible camera or the IR camera can be used for tip-tilt correction depending on the science arm we choose. It is controlled by detecting the motion of the center of the gravity of fast readout images by either visible or IR camera. Alternatively, lucky imaging technique^{26,27} can be used for tip-tilt removal.

EMCCD visible science camera. iRobo-AO uses a $1 \text{ K} \times 1 \text{ K}$ EMCCD (Andor iXon3 888) with $13\text{-}\mu\text{m}$ pixel size as the science camera in the visible arm (0.4 to $0.9 \mu\text{m}$). The camera can function both in single and in rapid frame modes with different predefined EM gain. There are a total of 16 preset modes in which the camera can operate and this also includes tip-tilt mode. The fast readout of the camera (~ 9 full frames per second) enables tip-tilt correction even without the IR camera. The data are stored in fits cube format and is processed with a shift and add lucky imaging algorithm.^{26,27} The plate scale and the field of view (FOV) are $2.25''/\text{mm}$ and $\pm 15''$.

Range gate. The beam from the laser projector is continuously Rayleigh scattered as it propagates upward through the atmosphere. To pick up the scattered light only from within the Rayleigh depth and to stop the stray scattered light from reaching the WFS, a range gating system²⁸ is installed. The gating works by opening a high-speed electro-optical shutter based on Pockels effect for a specific time such that only the scattered light from the Rayleigh depth reaches the WFS. More details are given in Sec. 2.3.3. The gating system is coupled with a delay generator (DG) to account for the return time of the pulse and can be individually programmed for delay and pulse width adjustments.

Wavefront sensor. iRobo-AO uses a Shack–Hartmann lenslet array for a WFS, which is made of a rectangular array of 11×11 planoconvex lenslets, each with a focal length of 76.6 mm and pitch of 0.5 mm. It is placed immediately after the Pockels cell. The wavefront sensing camera has an e2v CCD39 chip, which has 80×80 pixels each of size $24 \mu\text{m}$. There are four amplifiers at four corners of the CCD39, which can be read simultaneously for fast readout. More details on the wavefront sensing structure of the CCD39 camera are presented in Sec. 3. The plate scale and the FOV/subaperture are $0.675''/\text{pixel}$ and $4''$.

2.3.1 Optical relay

As shown in Fig. 10, the incoming light from the telescope is first directed perpendicular to the telescope axis with the help of an FM1 and the telescope entrance pupil is first reimaged on the DM with OAP1. After reflection from the DM and with the help of a dichroic filter (UV dichroic), all the UV light is reflected toward the wavefront sensing arm. The transmitted visible and IR beam after reflection from OAP2 and OAP3 passes through the ADC and is guided by the TTM to OAP4. Finally with the help of another dichroic filter (science dichroic) the visible light is passed to the EMCCD and the IR light to the IR camera.

In the UV arm, with the help of a lens and OAP5, the pupil is again reimaged on the SHWFS after passing through the range gating system. The range gating system is mounted between two crossed polarizing beam splitters (PBSs). A rotating half waveplate retarder at the entrance of the first PBS keeps the polarization axis of the LGS light fixed with respect to the axis of the



Fig. 12 Mechanical assembly of iRobo-AO.

polarization components following it. The range gating system is discussed in detail in Sec. 2.3.3. Finally, the image after the SHWFS is relayed to the CCD39 with a pair of relay lenses. Figure 10 shows the complete optical relay, and the complete mechanical assembly of iRobo-AO is shown in Fig. 12.

Optical performance. With a $f/45.42$ beam and a plate scale $2.25''/\text{mm}$ at the input of the EMCCD, a theoretical estimate of the FWHM at $\lambda = 0.65 \mu\text{m}$ is $\sim 30.4 \mu\text{m}$ or 2.34 pixels,

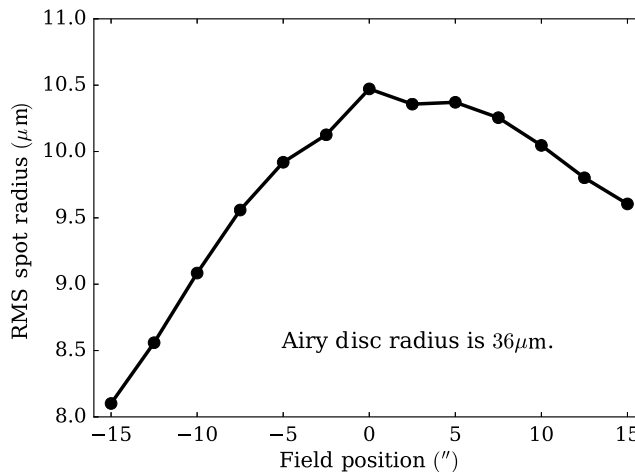


Fig. 14 RMS spot size variation at EMCCD with field position.

which satisfies the Nyquist criteria. Figure 13 shows the polychromatic spot diagram on the EMCCD for a total FOV of $\pm 15''$. The variation of the RMS spot size at EMCCD as a function of field position is given in Fig. 14.

In the UV arm, the most important parameter other than the pupil diameter on the SHWFS is the wavefront error and the

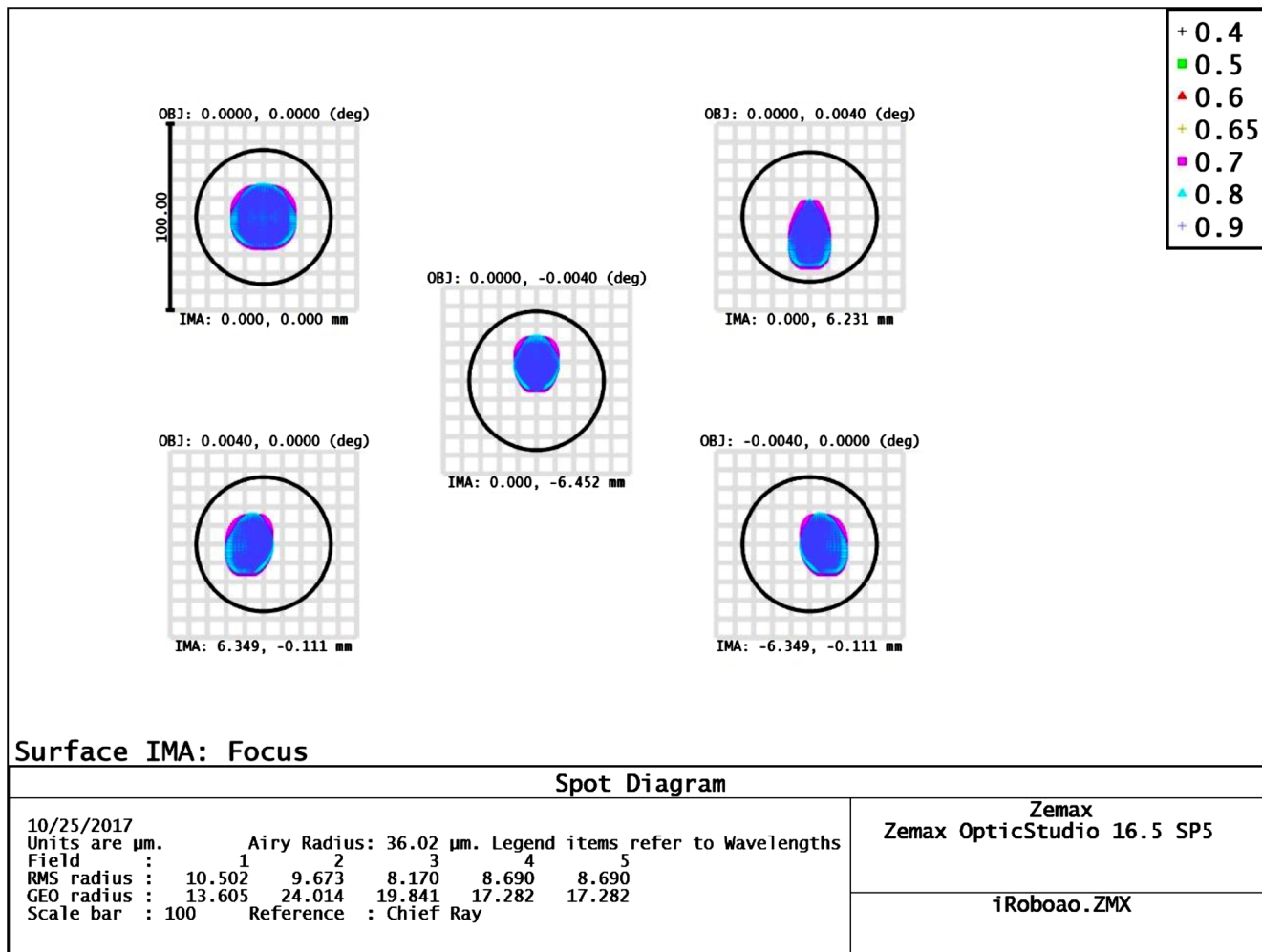


Fig. 13 Polychromatic spot diagram on EMCCD.

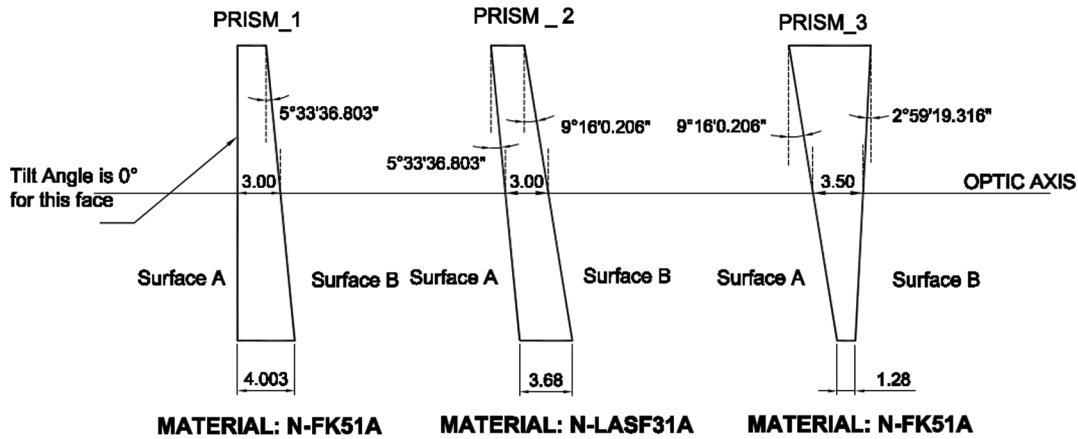


Fig. 15 ADC unit has two identical cemented prisms, each of which has three components as shown (dimensions are in millimeters).

degree of collimation of the beam. After several rounds of iteration of the lens (after UV dichroic) and OAP5 parameters, we obtain a 0.5" collimated beam with a tilt removed P-V and RMS wavefront error of 0.04λ and 0.0072λ at $0.355 \mu\text{m}$.

2.3.2 Atmospheric dispersion corrector

Apart from astronomical seeing, the other deleterious effect of the Earth's atmosphere on the light that passes through it is caused by atmospheric dispersion. Atmospheric dispersion smears out the light into different wavelengths due to differential refraction as light passes through the atmosphere. Atmospheric dispersion is a cumulative effect of pressure, temperature, humidity, and location of the observatory, but the altitude of the object has the maximum effect on dispersion; the lower the object (farther away from zenith), the more is the dispersion, as light passes through a thicker layer of the atmosphere.

The net effect of dispersion is elongation of the object's image on the camera, leading to a loss of resolution thereby defeating the purpose of AO. ADCs, therefore, play a very important role in AO systems.

Among the many types of ADC designs, the rotating double Amici prism design is most widely used in astronomy.^{29,30}

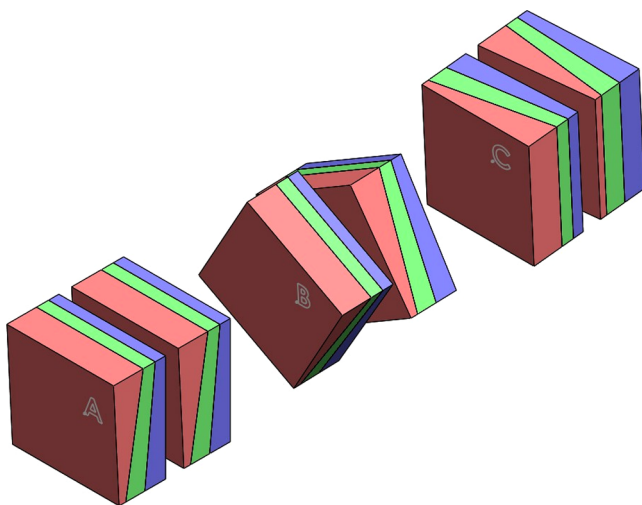


Fig. 16 Illustration of the relation of prism angle to zenith angles for three cases, A, B, and C with prism angles 0 deg, 30 deg, 90 deg, and zenith angles 65 deg, 61.8 deg, and 0 deg in sequence.

Design. As shown in Fig. 16, it consists of two identical prism assemblies, each capable of rotating independently about the optic axis. Each of our prism assemblies consists of cemented wedge-shaped glass plates (Fig. 15), made of N-FK51A, N-LASF31A, and N-FK51A in sequence. These glasses have good transmission over the working wavelength range. For maximum, intermediate, and minimum dispersions, the orientation of the prisms are shown in Fig. 16. The beam diameter at ADC is $\approx 10 \text{ mm}$. To minimize the reflection losses, the exposed surfaces were antireflection-coated. The optical design of the ADC was done using Zemax, and to take atmospheric parameters into account we used the Zemax subroutine "Atmospheric" (this subroutine simulates the effects of the refraction through the Earth's atmosphere when viewing a point source or a star). It is designed to work across the wavelength range from 0.4 to $2.2 \mu\text{m}$.

The performance of the design over the entire working wavelength range is shown in Fig. 17. The polychromatic RMS spot size is well within the Airy disk radius of $12 \mu\text{m}$ (defined at an intermediate wavelength of $1 \mu\text{m}$) for various zenith angles (z) of the object. Similar behavior is also obtained in the individual B, V, R, I, J, H, and K bands. From the figure, we also infer that at $z \approx 65 \text{ deg}$ (maximum dispersion case), the prisms get aligned with prism angle (θ) $\sim 0 \text{ deg}$ and the dispersion of

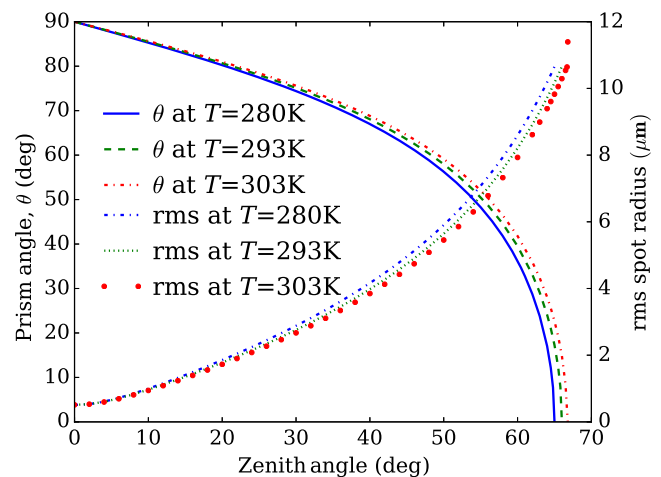


Fig. 17 The optimal prism angle and the RMS spot size for three working temperatures, as function of zenith angle.

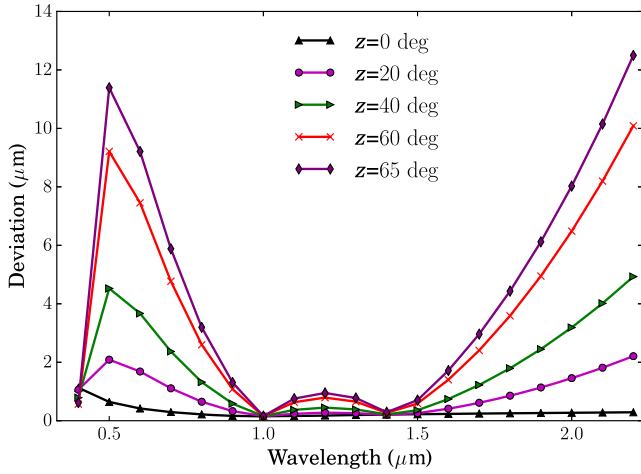


Fig. 18 Deviation of monochromatic spot position over the working wavelength band as a function of different zenith angle (z) at $T = 280$ K.

individual prisms adds up in a manner nullifying the atmospheric dispersion.

A plot for the deviation of monochromatic spot position from the reference position (i.e., the position of the primary wavelength at $1 \mu\text{m}$) versus wavelength at the optimal prism angle for various zenith angles are given in Fig. 18. All spots sizes are well within the Airy disk.

The analysis was done with the IGO specific parameters for observatory height, pressure, humidity, and latitude of 1005 m, 993 mbar, 50%, and 19.0883°N , and three different temperatures.

Relation between prism angle and dispersion. The atmospheric angular dispersion between wavelengths λ_{max} and λ_{min} at a particular location and object position can be defined as

$$D_{\text{atm}} = \xi_{\lambda_{\text{max}}} - \xi_{\lambda_{\text{min}}}, \quad (11)$$

where ξ_{λ} is the net bending of light from upper atmosphere to the observer at λ . Assuming p to be the dispersion of individual prisms, which are rotated by $\pm\theta$ (one prism rotates by $+\theta$ and the other rotates by $-\theta$ and the differential angle between the two prisms is 2θ) from a nominal position, it can be shown using vector addition equation³¹ that the dispersion of the ADC can be given as

$$D_{\text{adc}} = 2p \cos(\theta). \quad (12)$$

This expression can be inverted to estimate the prism rotation angle θ for a particular D as

$$\theta = \cos^{-1}\left(\frac{D_{\text{adc}}}{2p}\right). \quad (13)$$

The analytical method of estimating D_{atm} is discussed in Sec. 2.3.2. To nullify the atmospheric dispersion, D_{adc} must be equal to D_{atm} but opposite in sign.

Laboratory performance of ADC. To check laboratory performance of the ADC, dispersion data points were obtained experimentally and with Zemax between wavelengths 0.355 and $0.556 \mu\text{m}$ by rotating the prisms from 0 deg to 90 deg. Atmospheric effects were not considered here. In Fig. 19, the dispersion of the ADC at various prism angles obtained from

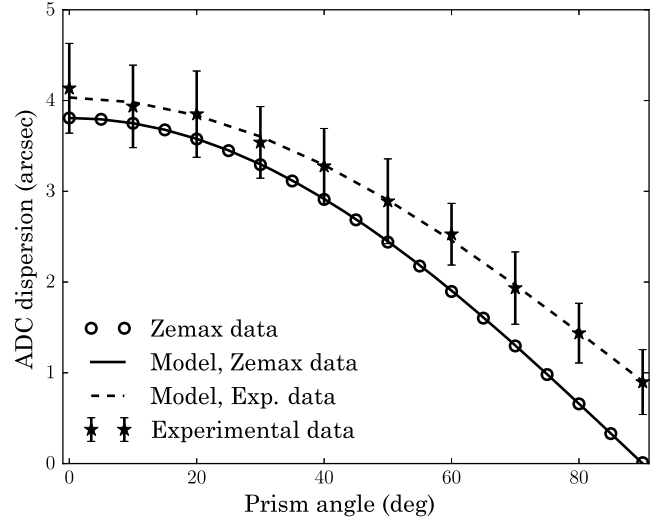


Fig. 19 Comparison of laboratory performance of ADC with Zemax.

Zemax (Zemax Data) are superposed with dispersion data obtained from Eq. 12 (model, Zemax data) with $p \sim 1.9039''$, where the dispersion of individual prism was again estimated from Zemax. To fit the laboratory data, a dispersion equation in more general form was written as

$$D_{\text{adc}} = dc + 2p_{\text{exp}} \cos(\theta + \phi), \quad (14)$$

where the term dc and epoch ϕ were introduced in Eq. (14). This model was fitted (model, exp. data) to the laboratory data (experimental data) from which we obtain $p_{\text{exp}} \sim 1.548543'' \pm 0.057332''$, $\phi \sim 0.557698 \text{ deg} \pm 2.525664 \text{ deg}$, and $dc \sim 0.936802'' \pm 0.155637''$.

Difference between the experimental data and the Zemax prediction, as seen from Fig. 19, can be attributed to alignment errors, minor difference in refractive indices of the melt glasses with that of the indices of Zemax glass catalog, and due to minor fabrication error particularly in the wedge angles of the prisms.

Estimation of atmospheric dispersion: We discuss two cases here.

Fixed atmospheric parameters. Following Smart and Green,³² we assume an atmospheric dispersion model as

$$D_{\text{atm}} \propto \tan(z). \quad (15)$$

Equating Eq. (15) to Eq. (12), it can be shown that

$$\frac{\cos(\theta)}{\tan(z)} = k, \quad (16)$$

where k is the proportionality constant. Rearranging,

$$\theta = \cos^{-1}[k \tan(z)]. \quad (17)$$

Using the optimized values of θ for various z from Fig. 17 in Eq. (16), the mean value of k was estimated to be 0.466 for $T = 280$ K. Figure 20 shows a good match between Eq. (17) and the data points of Fig. 17. Similar behavior is noticed at other temperatures but with different values of k . As the value of k changes with varying temperature throughout the night, this method sets serious constraints on the estimated value of D_{atm} . One, therefore, needs to look at more generic methods of

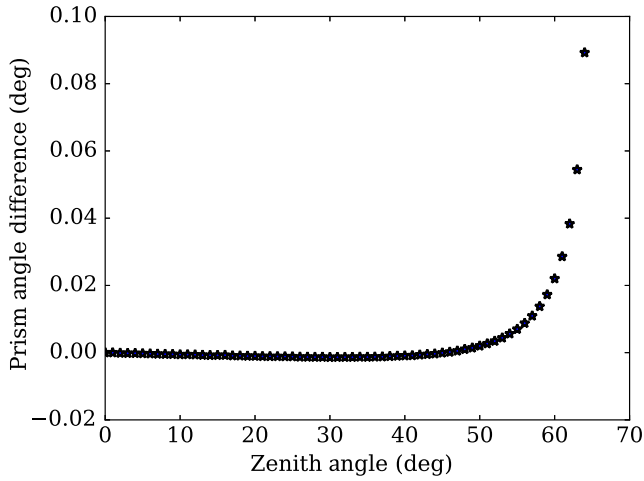


Fig. 20 Difference of prism angle obtained from Zemax and model at $T = 280$ K.

estimating D_{atm} using atmospheric parameters only and also take into account their real-time variation.

Varying atmospheric parameters. Here, we estimate D_{atm} following the atmospheric model proposed by Sinclair³³ and Hohenkerk et al.³⁴ All the atmospheric and object parameters are stored in a file, which can be updated at regular intervals and called by the computer program that calculates the required prism rotation angle. The program can also accommodate all observatory-related parameters, thus making it versatile enough to be used at any observatory. Computing D_{atm} for a set of atmospheric parameters (as in Sec. 2.3.2) and using Eq. (13) with $p \sim 2.266''$ for the entire working wavelength range, we obtain θ for various z , as shown in Fig. 21. To accommodate for the slight mismatch (this mismatch is unrelated to the results of the laboratory measurements mentioned in Laboratory performance of ADC paragraph) at higher values of z , we slightly modified the expression for A [the variable A is part of the expression (Cauchy's equation) of the refractive index of air in the troposphere] in the troposphere region³⁴ with a factor 0.92257. The final expression can be written as

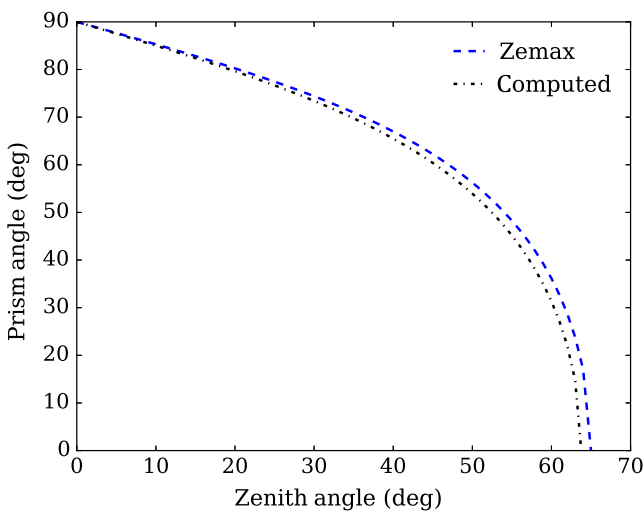


Fig. 21 Comparison of computed data following NAO technical note with Zemax at $T = 280$ K.

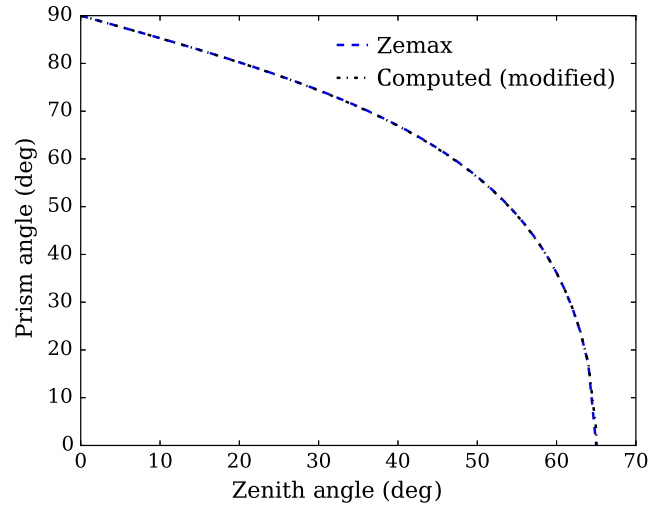


Fig. 22 Comparison of computed data following NAO technical note with Zemax at $T = 280$ K after modification.

$$A = 0.92257 \left(287.604 + \frac{1.6288}{\lambda^2} + \frac{0.0136}{\lambda^4} \right) \frac{273.15}{1013.25}. \quad (18)$$

Figure 22 shows a good match between the computed values and the Zemax data points. We adopted this algorithm to drive the iRobo-AO ADC unit.

Effect of telescope derotator. When an altitude azimuth telescope (as in IGO) is pointed exactly toward the North (South) direction (azimuth angle 0 or π), the elevation axis moves along a line of constant RA and a change in telescope elevation produces only a change in declination. For any other azimuth orientation, there is some angular difference between a line of constant RA and the line accessed by moving the telescope in elevation; this angle is known as the parallactic angle. Thus, the parallactic angle is the angle between a line of constant azimuth and a line of constant RA. Lines of constant azimuth converge at the zenith and lines of constant RA converge at the projection of the Earth's North Pole on the sky.

Also, when an alt-azimuth telescope tracks an object field, the image of that field rotates with time. The object field orientation on the focal plane is kept steady by moving the derotator by an angle equal to the parallactic angle.³⁵

At the Cassegrain focus of an alt-azimuth telescope, the mid-angle of the two prisms has to remain fixed relative to the telescope tube, as the dispersion direction is always perpendicular to the elevation axis. As the ADC unit is located behind the derotator, the entire unit will rotate relative to the telescope tube. Prism 1 and the prism 2 are mounted on two independent rotation stages. So to keep the mid-angle of the prisms fixed relative to the dispersion axis, we have to rotate both the prisms in exactly the opposite direction as the derotator by an amount equal to the parallactic angle. This is in addition to the differential prism angles required for dispersion correction. The prism angle (θ) is the theoretical angle of the prism calculated from Eq. (17). The net rotation angle of the stages of prism 1 and prism 2 would then be³⁶

$$\Omega_1 = \theta - \omega_{pa} + \text{offset}_1, \quad (19)$$

$$\Omega_2 = -\theta - \omega_{pa} + \text{offset}_2, \quad (20)$$

respectively, where ω_{pa} is the parallactic angle and offsets (offset_1 , offset_2 of the two prisms stages) are the difference between the actual mechanical and the theoretical estimated prism angle ($\Omega - \theta$) corresponds to, when $\omega_{pa} = 0$, which is when the object crosses the meridian. The signs of the angles in Eqs. (19) and (20) are best estimated on-sky. A computer program estimates ω_{pa} and θ and updates Ω at a rate discussed in the next section.

Rate of rotation. As it is not desirable for the prisms to lag behind in time from the stipulated positions, an estimate of the optimal rotation rate needs to be done. For $k = 0.466$, from Eq. (17) and Smart and Green³² we obtain [the rate of change of hour angle is $\frac{360 \text{ deg}}{23^h 56^m 04.0905^s} = \frac{15}{3600} (1 + \frac{1}{365.2422}) \text{ deg/s}$, neglecting higher-order terms]

$$\frac{d\Omega_1}{dt} = \frac{d\theta}{dt} - \frac{d\omega_{pa}}{dt}, \quad (21)$$

$$\begin{aligned} \frac{d\theta}{dt} &= \frac{d\theta}{dz} \frac{dz}{dt} \\ \frac{d\theta}{dz} &= -\frac{k \sec^2(z)}{\sqrt{1 - [k \tan(z)]^2}} \\ \frac{dz}{dt} &= \frac{15}{3600} \left(1 + \frac{1}{365.2422}\right) \sin A \cos \phi \text{ deg/s} \\ \frac{d\theta}{dt} &= -\frac{15}{3600} \left(1 + \frac{1}{365.2422}\right) \left[\frac{k \sec^2(z)}{\sqrt{1 - [k \tan(z)]^2}} \right] \\ &\quad \times \sin A \cos \phi \text{ deg/s}, \end{aligned} \quad (22)$$

and

$$\frac{d\omega_{pa}}{dt} = -\frac{15}{3600} \left(1 + \frac{1}{365.2422}\right) \cos \phi \cos A \operatorname{cosec}(z) \text{ deg/s}, \quad (23)$$

$$\begin{aligned} \frac{d\Omega_1}{dt} &= \frac{1}{240} \left(1 + \frac{1}{365.2422}\right) \left[-\frac{k \sec^2(z)}{\sqrt{1 - [k \tan(z)]^2}} \right. \\ &\quad \left. \times \sin A + \cos A \operatorname{cosec}(z) \right] \cos \phi \text{ deg/s}, \end{aligned} \quad (24)$$

where A and ϕ are the azimuth angle and latitude, respectively. Using Eqs. (19), (22), and (23), an estimate of the rate of rotation for one prism stage [Eq. (24)] is shown in Fig. 23 for $T = 280 \text{ K}$, where the mean value of k is larger as compared to $T = 293 \text{ K}$ and $T = 303 \text{ K}$. The other prism angle (Ω_2) changes in a similar fashion but with the opposite sign. It is seen that the required maximum rate of rotation is $\sim 0.28 \text{ deg/s}$, and the default speed of the ADC rotational stages have been set to 2.0 deg/s which is much above the estimated maximum value.

The ADC moves at the set default maximum speed quickly and stops and waits about 3 s until the next update. The maximum mismatch of around 0.84 deg ($= 0.28 \text{ deg} \times 3$) between the required and the achieved positions occurs at the maximum zenith angle (z) $\approx 65 \text{ deg}$ in the 3-s interval. The RMS and geometrical spot radius changes are well within the Airy disk due to the mismatch up to $\pm 2 \text{ deg}$ prism angle (Fig. 24), which justifies the 3-s update frequency.

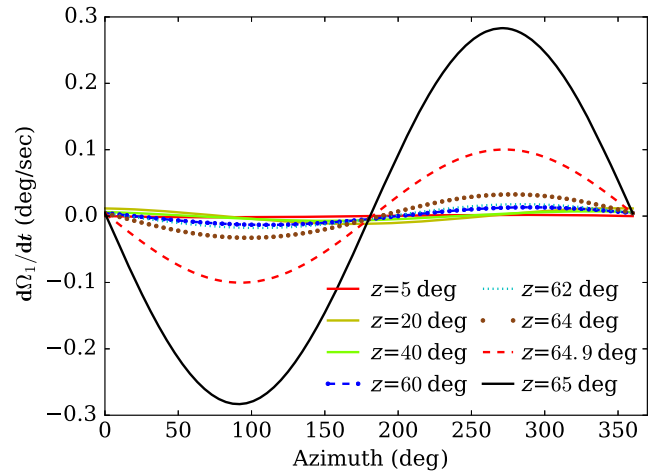


Fig. 23 Rate of rotation of the ADC prism for various azimuth and zenith angles.

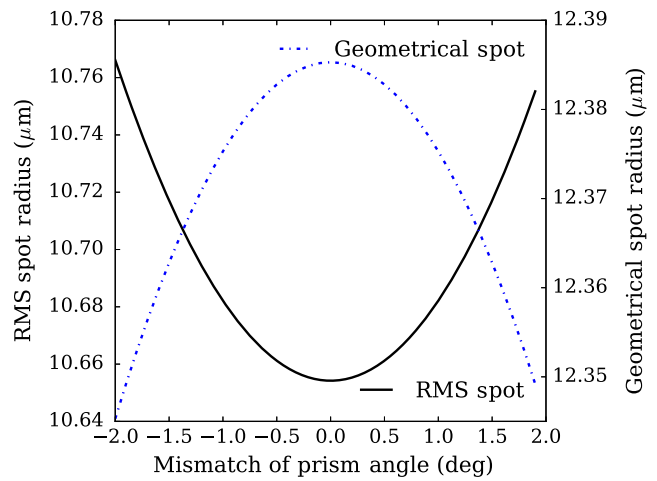


Fig. 24 Spot variation due to mismatch of the required and achieved prism angle at 65-deg zenith angle.

2.3.3 Range gate

At the heart of the LGS-based AO system is a 10-W Q-switched UV pulse laser with a pulse width of 33 ns and 10-kHz repetition rate. The Q-switched signal from the laser is fed to the pulse DG, which triggers the ON/OFF states of the Pockels cell electro-optical shutter. When the appropriate voltage is applied to the Pockels cell, it behaves like a half wave optical retarder in the optical path. The Pockels cell is placed between two orthogonal PBSs. When a voltage as high as 3.3 kV (for 355 nm) is applied to the Pockels cell, the shutter switches to “open” mode and the beta- BaB_2O_4 crystal of the Pockels cell rotates the plane of polarization of the input beam by 90 deg, which can pass through the orthogonal PBS. When no voltage is applied to the crystal, the light is blocked by the crossed PBS.

The shutter was first carefully aligned on an optical bench to ensure that the laser beam transits the crystal parallel to the direction of the crystal’s Z axis. A commercial laser was first made parallel to the optical bench, and later the crystal was inserted in the optical path. Fine adjustment with precision gimbal mount was made to ensure that the crystal axis and the laser axis are collinear, which can be determined by isogyres seen on a screen as shown in Fig. 25.

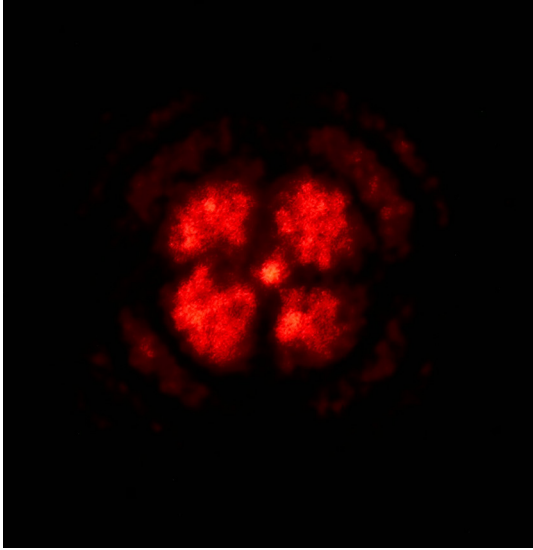


Fig. 25 Isogyres as seen on a screen.

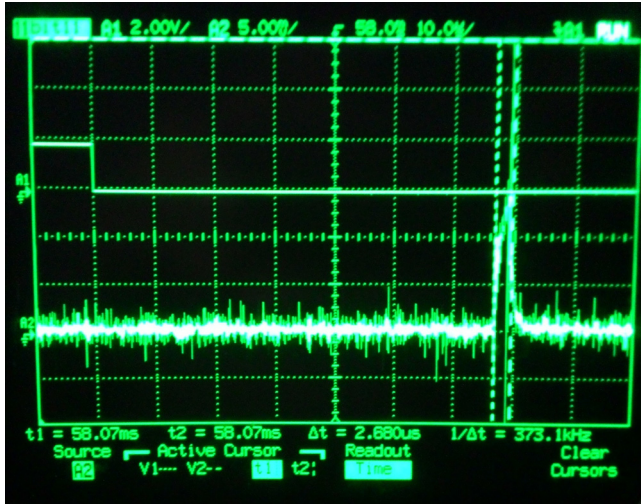


Fig. 26 A gated pulse width of $2.3 \mu\text{s}$ picked up by the photodiode using a function generator (time/major division: $10 \mu\text{s}/\text{division}$).

To check the behavior of the shutter when voltage is applied to it, we triggered the DG with 500-Hz square signal from a function generator. The output ON/OFF signal from the DG triggers the ON/OFF state of the Pockels cell; the ON/OFF signals are separated by $2.3 \mu\text{s}$ (corresponding to 345 m on sky, which is the expected height of laser “spot”), whereas the time delay between the DG ON and the signal from the function generator was set to $66.67 \mu\text{s}$ (corresponding to beam return time from 10-km altitude in the sky). A high-sensitive photodiode was used to pick up the gated signal from the Pockels cell, as shown in Fig. 26.

Cassegrain derotator effect. As the laser projector is located at the side of the telescope that has an alt-azimuth mount system, the Cassegrain derotator causes the polarization plane of the laser beam (as seen by the Pockels cell) to change with time. However, the Pockels cell works only when the plane of polarization of the input beam is oriented in a particular direction with respect to the axes of the crystal. To ensure that this happens, an optical half waveplate retarder mounted on a rotating stage is

introduced at the entrance of the range gate system. The retarder is rotated so as to align the plane of polarization of the input laser beam to its original optimal direction every 3 s. The rate of rotation of the retarder is synchronized with that of the Cassegrain derotator.

As the same controller module drives both the ADC and the retarder mount, while each has different working principles, multithreading feature was introduced in the software structure to communicate with both the modules simultaneously.

New features. The entire instrument is optimized for IUCAA 2-m alt-azimuth system at Cassegrain main port, whereas the first Robo-AO was designed for equatorial-mounted 1.5-m Palomar P60 telescope. In the process, all the major optical components had to be redesigned to meet the iRobo-AO requirement, as given in Table 3. The significant differences are the incorporation of retarder in front of the Pockels cell to suit our alt-azimuth telescope requirement and the generic atmospheric parameter-sensitive ADC software. Both the components ADC and retarder work in sync and are driven by the same master controller.

3 Wavefront Reconstruction

The DM, the SHWFS, and the WFS camera are at first aligned as per the geometry shown in Fig. 27. The output of the WFS camera is a 3×3 binned image of size 26×26 binned pixels. There are 13×13 subapertures on an image, out of which only 11×11 subapertures are within the pupil and among them only 97 subapertures are used for the AO correction. The rest are unused because they do not contribute in wavefront sensing over the circular pupil. Each subaperture consists of 2×2 binned camera pixels. An unbinned image of the spot array formed by the SHWFS lenslets as seen on the WFS camera is shown in Fig. 28 after complete alignment of the wavefront sensing arm.

From each new image grabbed by the WFS camera, a linear array of pixel values is formed from which the wavefront slopes are measured. The x and y slopes of the images within each subaperture are measured as⁴

$$S_x = \frac{(I_2 + I_4) - (I_1 + I_3)}{(I_1 + I_2 + I_3 + I_4)}, \quad (25)$$

$$S_y = \frac{(I_3 + I_4) - (I_1 + I_2)}{(I_1 + I_2 + I_3 + I_4)}, \quad (26)$$

where the intensity at each pixel are numbered in a quadrant cell format as

$$\begin{pmatrix} I_3 & I_4 \\ I_1 & I_2 \end{pmatrix}. \quad (27)$$

As the response of a quadrant cell is nonlinear in nature particularly when it reaches the edges, the slopes are first linearized with the help of a precalculated table. Noncommon path errors are taken care of with the help of slope offsets, where again all the slope offsets are stored in a precalculated table. The final slopes are then multiplied by the reconstruction matrix to generate new DM actuator poke voltages as per the control law

$$P(t+T) = P(t) + gE(t) + I\{F - [P(t) + gE(t)]\}, \quad (28)$$

where $P(t+T)$ denotes the new position of the DM actuator, $P(t)$ denotes the current position of the DM actuator, $E(t)$

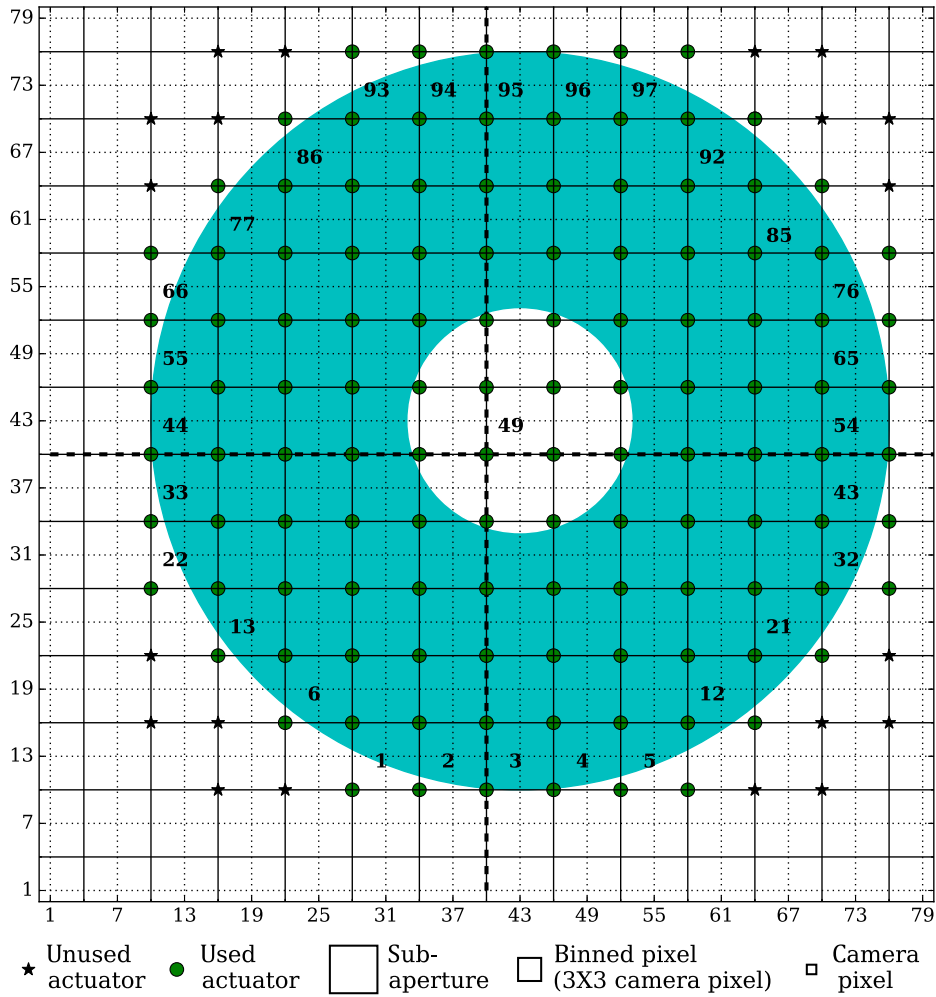


Fig. 27 Mapping of DM actuators and SHWFS lenslets as seen on WFS camera, the annular region represents the pupil size with secondary obscuration and each subaperture consists of 2×2 binned pixels. One binned pixel consists of 3×3 camera pixels.

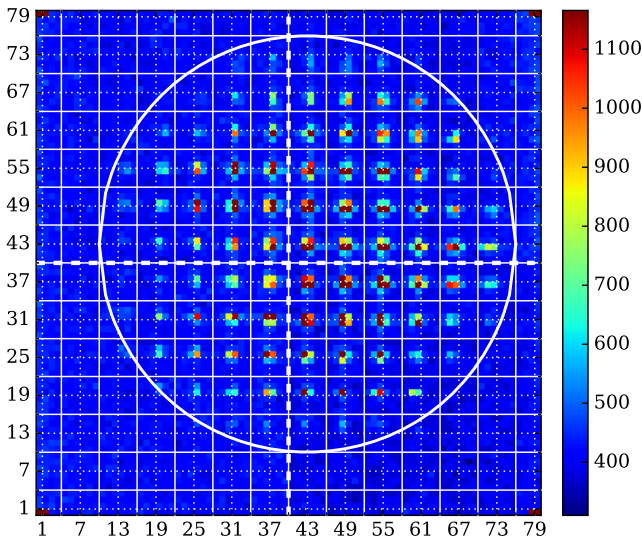


Fig. 28 Unbinned image of the spot array formed by SHWFS lenslets as seen on the WFS camera, the squares (solid line) and circle are representation of the subaperture and the telescope pupil.

denotes the errors after matrix multiplication, and F is the flatmap values of the DM describing its flat position. Here, g and l are the loop gain and leak constant.³¹ For small l , and in the absence of any measurement error, the system has a very small tendency to fall back to the flatmap values.

3.1 AO Loop

Figure 29 depicts the control structure of iRobo-AO. To check the behavior of the AO system, we ran the AO loop for some time with and without loop correction for comparison. The local X and Y slopes of the spots within each subaperture of the binned image were estimated and stored in the slope telemetry file (Fig. 29). This was done for all the 97 subapertures and in all the image frames captured within the specific runtime.

Figure 30 shows the RMS values of a set of 97 slopes against the individual frame numbers for both the cases, when AO correction was (i) absent and (ii) present. We present the data from three test runs in Fig. 30. Table 4 represents the mean of slope RMS and the standard deviation of the data plots in the linear sections for all cases.

Case (i), panel (a) of Fig. 30 represents the RMS variation of X and Y slopes when there is no AO correction.

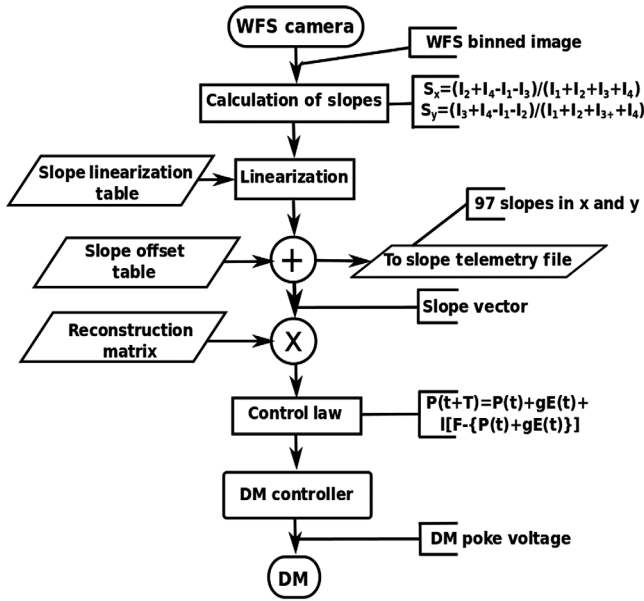


Fig. 29 Control flowchart of iRobo-AO.

Case (iia), panel (b) of Fig. 30 represents the RMS variation of slopes when the AO loop correction was turned on. The entire time plot is segmented into two parts, the initial system transient (S1) and steady-state part (S2), as shown in Fig. 30. We can see the servo effect, i.e., oscillation at the beginning of the system (transient state) at the S1 segment; this could be due to the presence of local turbulence. The RMS value in the transient became high and drastically reduced within the first few thousand frames. Then it reaches the steady state only with very little or no effect, henceforth, resulting in a flat curve (S2 segment). As a result of the servo loop state transition, the system is trying to achieve the target value from an OFF condition through the transient. Once the system reaches the target state, it locks and does not deviate from the target value. Thus, standard deviation reduces in locking period. Comparing Figs. 26(a) and 26(b) and results from Table 4, we find >70% reduction in slope deviation in X and Y, and the relative shift between means of X and Y slope RMSs in Fig. 26(b) is less by 80%, as compared to Fig. 26(a).

Case (iib): to test the system under a more rigorous condition, we generated artificial turbulence in the beam path, and this was done by passing ~1 A current through a 5-W resistance. It was mounted at a location such that the local turbulence generated from heating of the resistance would disturb the collimated light in the path of the telescope simulator. This disturbance would be reflected as a severe shift of slopes on the WFS camera. After the AO loop ran for some time, the heater was switched on for a period of about 5 to 10 s only. The results are presented in Fig. 30(c). The entire time plot is segmented into four parts S3, S4, S5, and S6.

Here, S1 and S3 represent the system's initial transient part and S5 represents the turbulent zone generated due to heating of the resistance. S2, S4, and S6 are the corrected segments.

Servo oscillation is present at the beginning of the system at the S1 segment, which is brought down by the system within the first thousand frames similar to the panel (b). The region where the artificial turbulence begins is distinct and shows high disturbance of the slopes in segment S5; eventually, this effect was

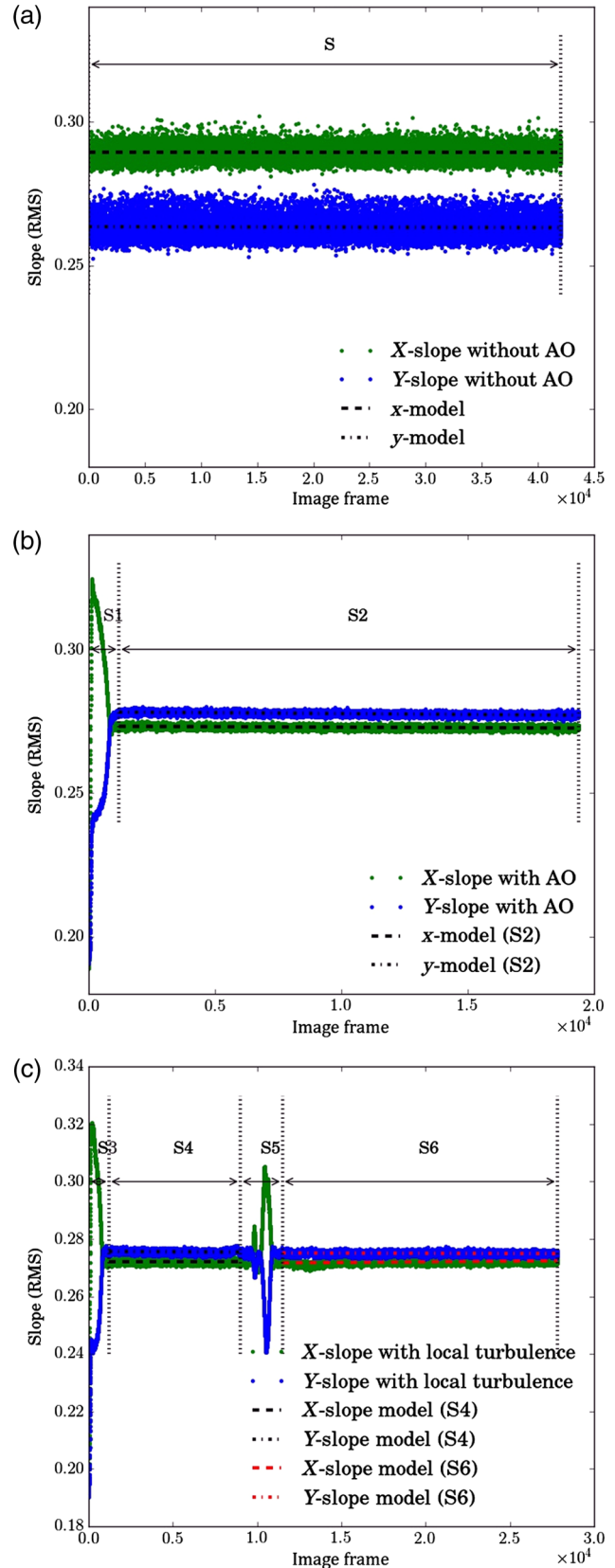


Fig. 30 (a), (b), and (c) The RMS variations of the slopes (dimensionless) with image frames in the absence AO correction, the presence of AO correction, and presence of AO correction under artificial turbulence, respectively.

Table 4 Statistics of data points in the linear sections.

Panel	Segment	Slope ^a	Mean of slope RMS	Standard deviation
(a) without AO	S	X-slope	2.894×10^{-1}	2.137×10^{-3}
		Y-slope	2.635×10^{-1}	2.832×10^{-3}
(b) with AO	S2	X-slope	2.733×10^{-1}	5.668×10^{-4}
		Y-slope	2.782×10^{-1}	6.181×10^{-4}
(c) with AO and turbulence	S4	X-slope	2.721×10^{-1}	5.330×10^{-4}
		Y-slope	2.757×10^{-1}	5.927×10^{-4}
	S6	X-slope	2.711×10^{-1}	6.325×10^{-4}
		Y-slope	2.753×10^{-1}	5.674×10^{-4}

^aSlope is dimensionless as per Eqs. (25) and (26).

also nullified quickly as we can see the fall of the slopes (in segment S6) due to the AO correction.

4 Conclusion

In this paper, we present the comprehensive design and description of the iRobo-AO instrument with various tests and calibration results obtained in the laboratory—a prerequisite before shifting it to the observatory.

In Sec. 2.1 to 2.2.2, we have presented the general description of the LGSF explaining all its internal components and their functions. The computed maximum elongation of coaxial and side projection of the LGS are 1.2" and 2", respectively. The importance of on-axis projection was also discussed with simulation results and how this was achieved at IGO with the help of periscopes.

Sections 2.3 to 2.3.1 discuss the Cassegrain AO facility with all its components. The optical performance of the system has been described at length; all the required optical and stroke size constraints required for AO correction at the IGO site were met. The net required stroke length of the DM actuator is 1.5 μm with separate tip-tilt correction, which is well within the 3.5- μm dynamic range of the used Boston Micromachines' MEMS-based DM.

Sections 2.3.2 to 2.3.3 discuss at length the ADC system designed with added features to suit the requirements of the IGO alt-azimuth telescope; some laboratory tests and modeling results under various atmospheric conditions were also presented. The ADC is designed to cope up with the atmospheric dispersion over the wavelength range from 0.4 to 2.2 μm up to ~ 66 deg zenith angle. The design produces reasonable 11.4- μm RMS spot radius, which is well within the 12 μm Airy disk radius shown in Fig. 17. The rate of rotation of the ADC mounts to counter the effects of Cassegrain derotator has also been discussed at length.

A method for reducing stray scattered light from reaching the WFS camera by gating the backscattered light of the LGS has been discussed in Sec. 2.3.3; optical alignment of the crystal and gating performance tests in the laboratory are also elaborated. The achieved range gating width is 2.3 μs , which corresponds to 345 m expected on-sky height of the laser "spot."

Finally in Sec. 3, we discuss the AO control law and how the corrected wavefront is reconstructed with some laboratory test

results under various conditions. The slope telemetry files are analyzed and plotted, and the AO correction is evident from the plots. About 70% reduction in the slope RMS deviation and about 80% reduction in the relative shift between the mean values of slope RMS in both X and Y were obtained with AO correction.

Acknowledgments

We sincerely thank Rani Bhandare, Deepa Modi, and Swapnil Prabhudesai for helping us in the process of procurement and fabrication of various components. We express our gratitude to Mandar Hulsurkar and Sakya Sinha for their generous help related to the software matters.

References

- H. W. Babcock, "The possibility of compensating astronomical seeing," *Publ. Astron. Soc. Pac.* **65**, 229 (1953).
- J. W. Hardy, J. Feinleib, and J. C. Wyant, "Real time phase correction of optical imaging systems," in *Digest of Tech. Pap. of the OSA Topical Meeting on Opt. Propag. Turbul.*, University of Colorado, Boulder, Colo (1974).
- J. W. Hardy, "Real-time wavefront correction system," U.S. Patent No. 3,923,400 (1975).
- J. W. Hardy, *Adaptive Optics for Astronomical Telescopes*, Oxford University Press, New York (1998).
- J. R. P. Angel, "Ground-based imaging of extrasolar planets using adaptive optics," *Nature* **368**, 203–207 (1994).
- R. L. Riddle et al., "The Robo-AO software: fully autonomous operation of a laser guide star adaptive optics and science system," *Proc. SPIE* **8447**, 84472O (2012).
- C. Baranec et al., "Bringing the visible universe into focus with Robo-AO," *J. Visual. Exp.* **72** (2013).
- C. Baranec et al., "High-efficiency autonomous laser adaptive optics," *Astrophys. J. Lett.* **790**, L8 (2014).
- R. Jensen-Clem et al., "The performance of the Robo-AO laser guide star adaptive optics system at the Kitt Peak 2.1-m Telescope," ArXiv e-prints (2017).
- C. Baranec, R. Riddle, and N. M. Law, "Automated adaptive optics," ArXiv e-prints (2017).
- N. M. Law et al., "Robotic laser adaptive optics imaging of 715 Kepler exoplanet candidates using Robo-AO," *Astrophys. J.* **791**, 35 (2014).
- C. Ziegler et al., "Robo-AO Kepler Planetary Candidate Survey. III. Adaptive optics imaging of 1629 Kepler exoplanet candidate host stars," *Astrophys. J.* **153**, 66 (2017).

13. R. Foy and A. Labeyrie, "Feasibility of adaptive telescope with laser probe," *Astron. Astrophys.* **152**, L29–L31 (1985).
14. C. E. Max et al., "Image improvement from a sodium-layer laser guide star adaptive optics system," *Science* **277**(5332), 1649–1652 (1997).
15. D. Summers et al., "Focus and pointing adjustments necessary for laser guide star adaptive optics at the W.M. Keck Observatory," *Proc. SPIE* **5490**, 1117–1128 (2004).
16. P. L. Wizinowich et al., "The w. m. keck observatory laser guide star adaptive optics system: overview," *Publ. Astron. Soc. Pac.* **118**(840), 297 (2006).
17. C. S. Gardner et al., "Lidar studies of the nighttime sodium layer over Urbana, Illinois. I—Seasonal and nocturnal variations," *J. Geophys. Res.* **91**, 13659–13673 (1986).
18. R. G. Rutten et al., "Facility class Rayleigh beacon AO system for the 4.2 m William Herschel Telescope," *Proc. SPIE* **4839**, 360 (2003).
19. O. Martin et al., "Optimisation of the range gating and calibration processes on the GLAS Rayleigh laser guide star at the WHT," *Proc. SPIE* **7015**, 70154E (2008).
20. C. Baranec et al., "Robo-AO: an autonomous laser adaptive optics and science system," in *Imaging and Applied Optics*, OSA Technical Digest (CD) Optical Society of America, p. 3 (2011).
21. M. Salama et al., "Robo-AO Kitt Peak: status of the system and deployment of a sub-electron readnoise IR camera to detect low-mass companions," *Proc. SPIE* **9909**, 99091A (2016).
22. L. Schreiber et al., "Laser guide stars for extremely large telescopes: efficient Shack-Hartmann wavefront sensor design using the weighted centre-of-gravity algorithm," *MNRAS* **396**, 1513–1521 (2009).
23. P.-Y. Madec, "Overview of deformable mirror technologies for adaptive optics and astronomy," *Proc. SPIE* **8447**, 844705 (2012).
24. R. J. Noll, "Zernike polynomials and atmospheric turbulence," *J. Opt. Soc. Am.* **66**, 207–211 (1976).
25. D. L. Fried, "Atmospheric turbulence optical effects: understanding the adaptive-optics implications," *NATO Adv. Sci. Inst. Ser. C* **423**, 25 (1994).
26. J.-L. Nieto and E. Thouvenot, "Recentring and selection of short-exposure images with photon-counting detectors. I—Reliability tests," *Astron. Astrophys.* **241**, 663–672 (1991).
27. N. M. Law, "Lucky imaging: diffraction-limited astronomy from the ground in the visible," *Observatory* **127**, 71–71 (2007).
28. R. Q. Fugate et al., "Laser Beacon adaptive optics with an unintensified CCD wavefront sensor and fiber optic synthesized array of silicon avalanche photodiodes for fast guiding," in *European Southern Observatory Conference and Workshop Proceedings*, Vol. 48, p. 487 (1994).
29. C. G. Wynne and S. P. Worswick, "Atmospheric dispersion correctors at the Cassegrain focus," *Mon. Not. R. Astron. Soc.* **220**, 657–670 (1986).
30. C. G. Wynne, "Correction of atmospheric dispersion in the infrared," *Mon. Not. R. Astron. Soc.* **282**, 863–867 (1996).
31. S. P. Tendulkar, "Beyond the blur," PhD Thesis, California Institute of Technology (2014).
32. W. Smart and R. Green, *Textbook on Spherical Astronomy*, Cambridge University Press, Cambridge (1977).
33. A. Sinclair, *The Effect of Atmospheric Refraction on Laser Ranging Data*, H.M. Nautical Almanac Office (1982).
34. C. Hohenkerk et al., *The Computation of an Angular Atmospheric Refraction at Large Zenith Angles*, H.M. Stationery Office (1985).
35. G. Schmidt, "Pointing/Derotor Coalignment for Alt-AZ Telescopes," in *MMTO Internal Technical Memorandum 04-1* (2004).
36. S. Egner et al., "Atmospheric dispersion correction for the Subaru AO system," *Proc. SPIE* **7736**, 77364V (2010).

Biographies of the authors are not available.